Metals & corrosion

High-temperature oxidation behaviour of additively manufactured and wrought HAYNES 282

Mateusz Kopec[1,*] , Izabela Mierzejewska[1,2], Dominika Gorniewicz[2], Ryszard Sitek[3], and Stanisław Jóźwiak[2]

[1] *Institute of Fundamental Technological Research, Polish Academy of Sciences, Pawińskiego 5B, 02-106 Warsaw, Poland*
[2] *Military University of Technology, Faculty of Advanced Technologies and Chemistry, 00-908 Warsaw, Poland*
[3] *Warsaw University of Technology, Faculty of Materials Science and Engineering, Wołoska 141, 02-507 Warsaw, Poland*

ABSTRACT

Direct Metal Laser Sintered Haynes 282 specimens as well as wrought ones were subjected to high-temperature exposure at 1000 °C for 100h in air to compare their oxidation behaviour. The specimens were removed from the furnace after 1h, 5h, 25h, 50h and 100h to reveal and study oxidation mechanisms through morphological and cross-sectional examination by using scanning electron microscopy with energy dispersive spectroscopy attachment and X-ray diffraction. Microstructural studies revealed that the oxidation kinetics, determined by changes in thickness scale and depth of aluminium diffusion zone, were mainly driven by the formation of Cr_2O_3 for the wrought material, and TiO_2 for DMLS one. The wrought material was characterized by the oxidation rate equal to 0.96 and followed the logarithmic law. On the other hand, DMLS-manufactured Haynes 282 exhibited oxidation rate of 0.90 and follows the linear law for the thickness scale considerations. However, when the depth of aluminium diffusion was investigated, it had an oxidation rate of 0.87 and followed cubic law.

Introduction

High strength at elevated temperature, excellent corrosion and oxidation resistance, and good creep and fatigue performance of nickel-based superalloys have attracted attention in a diverse range of industries, such as aerospace, nuclear, and marine [1, 2]. These excellent mechanical properties are associated with a stable microstructure consisting of an austenitic (γ) matrix hardened through the solid solution by gamma-prime (γ') and gamma-double-prime (γ'') precipitates. Furthermore, nickel-based superalloys contain many stabilizing elements responsible for their great performance under extreme conditions [3]. The γ phase is stabilized by elements such as Co, Cr, Ru, Re, Mo, and W due to their atomic radii being similar to that of Ni.

Conversely, the γ' phase is stabilized by Al, Ta, and Ti, which have larger atomic radii. Additionally, in polycrystalline Ni-based superalloys, elements like B, C, and Zr segregate to grain boundaries and enhance their strength. Elements such as Ti, Ta, Nb, Re, W, Mo, and Cr act as solid solution strengtheners. Ta, Ti, and Nb specifically strengthen the γ' phase, while the remaining elements, known as refractory elements, strengthen the γ matrix [4]. Among nickel-based alloys, Haynes 282 is characterized by outstanding mechanical properties such as high creep strength at temperature up to 927 °C and an excellent combination of weldability and fabricability that surpass other nickel alloys [5]. Haynes 282 contains a relatively low volume fraction of γ' which guarantees a balance between strength at high temperature and fabricability [6]. One should mention, that nickel-based superalloys are susceptible to cracking during rapid solidification processes, including welding, due to their complex chemical compositions. However, Haynes 282 is distinguished by its superior resistance to this type of fracture [2]. Because of such resistance and superior mechanical properties, this material is promising for AM processes, as considerable cost savings during the manufacturing of complex-shaped components could be obtained [7]. Additionally, an excellent dimension precision level of additively manufactured nickel-based superalloys components could be achieved [8]. The unquestionable advantages of additively manufactured nickel-based superalloy parts are their enhanced mechanical properties originating from the grain refinement and reduced microsegregation and porosity commonly occurring during casting [7, 9].

DMLS is one of the AM techniques, that possesses several advantages. In this process, precise complex components could be directly fabricated through 3D computer-aided design (CAD) without moulds. Furthermore, the non-fused powder can be reused after sieving [10]. At the beginning of the DMLS process, a metal powder bed is applied on a metal plate by using a recoater blade. Subsequently, a thin layer of powder is sintered by using a laser beam of high intensity. As the plate position is lowered, the recoater arm deposits a new, 20 or 40 µm thick layer and the process is repeated until a complete 3D model of the part is built [11]. One should highlight a number of papers reporting different AM methods applied for Haynes 282. Otto et al. [12] optimized laser beam powder bed fusion (PBF-LB) technology in which the build platform is heated to 300°C

and a novel scan strategy was used to manufacture low porosity and micro-crack free material. Shaikh et al. [4] presented fully dense and crack-free Haynes 282 produced by Laser Powder Bed Fusion (LPBF). The manufactured material exhibited higher tensile properties at room temperature in comparison with wrought material, which was mainly caused by strengthening due to grain refinement. Maj et al. [13] reported improved mechanical properties of Haynes 282 obtained by using LPBF and hot pressing (HP) in comparison with wrought material. Kopec et al. [14] studied the suitability of the DMLS method to manufacture the Haynes 282. The authors found, that the AM process improved the fatigue response of the nickel-based alloy by 200 MPa as compared to the wrought material. Unocic et al. [2] reported comparable hardness and tensile strength of the as-fabricated electron beam melted (EBM) Haynes 282 in comparison with its wrought state. Ramakrishnan and Dinda [7] found, that the application of direct laser metal deposition for Haynes 282 enabled to improve the tensile characteristics of the as-deposited material as compared to the cast ones. It could be observed, that different AM processes could be successfully used to manufacture Haynes 282-based parts. Therefore, further steps should be taken to commercialize these methods for the industrial scale. Since this material in its wrought form is widely used for high-temperature applications, for example in the construction of advanced-ultra-supercritical power plant equipment, its oxidation behaviour should be investigated in detail [15, 16]. Perez-Gonzalez et al. [16] studied isothermal oxidation resistance of Haynes 282 in air using gravimetric methods within the temperature range of 800–1000 °C for up to 150 h. In such a study, the oxidation kinetics were described by the parabolic rate law. The scale's chemical composition consisted of an outer layer of TiO_2 and an inner layer of Cr_2O_3, with the latter situated at the interface between the metal and oxide. Furthermore, the presence of an internal oxidation zone containing Al_2O_3 and TiO_2 was observed at all temperatures. Tung et al. [17] reported that the high temperature oxidation of Haynes 282 at temperature up to 950°C resulted in layered chromium scale formation. Oxidation kinetics were parabolic and controlled by Cr diffusion. Microstructural studies performed on specimens' cross-sections revealed a continuous Cr_2O_3 layer and a layer of loose oxide rich in Co-Ti-Ni formed above the chromium. Nnaji

et al. [18] presented that Haynes 282 displayed a fairly rapid, linear/quasi-parabolic rate of oxidation ($n = 0.65$) at 1050 °C and ($n = 0.68$) at 1100 °C, which was attributed to the presence of chromium oxide containing some titanium oxides, that were further responsible for the formation of a more adherent oxide film.

Although there have been studies on high-temperature oxidation of wrought Haynes 282 in air, the performance of additively manufactured material under extreme conditions has not been investigated in detail as yet. Furthermore, despite the high microstructural stability and outstanding oxidation resistance of Haynes 282, its complex chemical composition significantly affects the formation of the internal and outer oxide layers at high temperature. Formation of these oxides also accounts for the reduction of the mechanical strength in the temperature range between 800°C and 1200°C, thus deep analysis of oxidation mechanisms is required to understand the phenomena responsible for their structural degradation.

In order to extend the current knowledge on the oxidation behaviour of Haynes 282 subjected to high temperature exposure in air, a detailed microstructural analysis was executed through SEM–EDS and XRD on the wrought specimens as well as those produced by the DMLS method. This paper also aims to evaluate the structural stability of additively manufactured Haynes 282 in relation to its as-cast state to assess its potential in structural applications.

Materials and methods

Haynes 282 specimens were manufactured by using DMLS, in which spherically shaped powder with an average diameter equal to 45µm was used (Fig. 1a). Cylindrical bars of 5mm in radius and 50mm long were printed by using EOS M100 machine on a substrate plate preheated to 80°C. The printing machine is equipped with Yb laser of maximum effective power equal to 200 W, wavelength of 1064 nm and laser spot of ~ 0.04 mm. The processing parameters were optimized as follows: an energy density of 104 J/mm^3, laser power of 100 W, laser speed of 800 mm/s, and the distance between successive paths of 0.05 mm. The specimens were printed with the orientation along the vertical axis.

The chemical composition of wrought and powder material is presented in Table 1. The composition of wrought material did not differ significantly from the results presented in Table 1. The dense structure of subsequent layers confirmed the appropriate selection of process parameters since a coherent microstructure with overlapping fusion pools was obtained in the parallel (Fig. 1b) and the perpendicular direction (Fig. 1c).
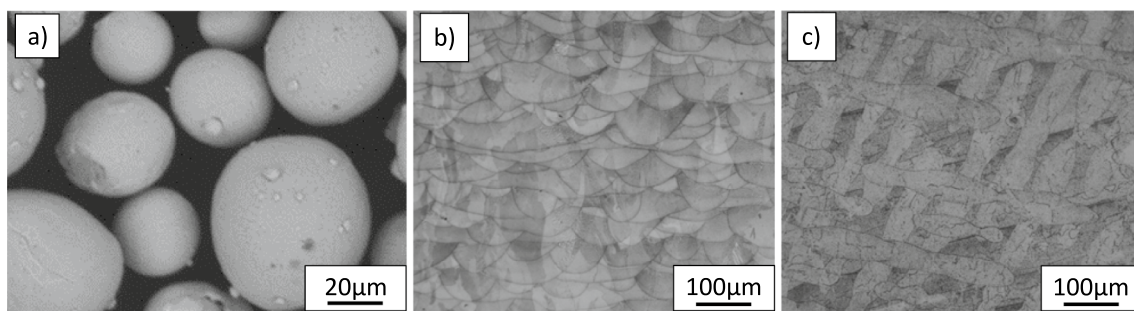

Figure 1 The micrograph of Haynes 282 powder (**a**); and microstructure of the as-built alloy observed along the parallel (**b**) and the perpendicular (**c**) to the building direction section.

Table 1 Chemical compositions of wrought Haynes 282 and its powder used in the DMLS process (Wt.%)

Element	Ni	Cr	Co	Mo	Ti	Fe	Al	Mn	Si	C
wrought	Bal	20.0	10.0	8.5	2.0	1.5	1.5	0.3	0.2	0.1
DMLS	Bal	19.5	10.0	8.5	2.1	1.5	1.5	0.3	0.2	0.1

Figure 2 The initial micro-structure and XRD graphs of wrought (**a**, **c**) and additively manufactured (**b**, **d**) Haynes 282.
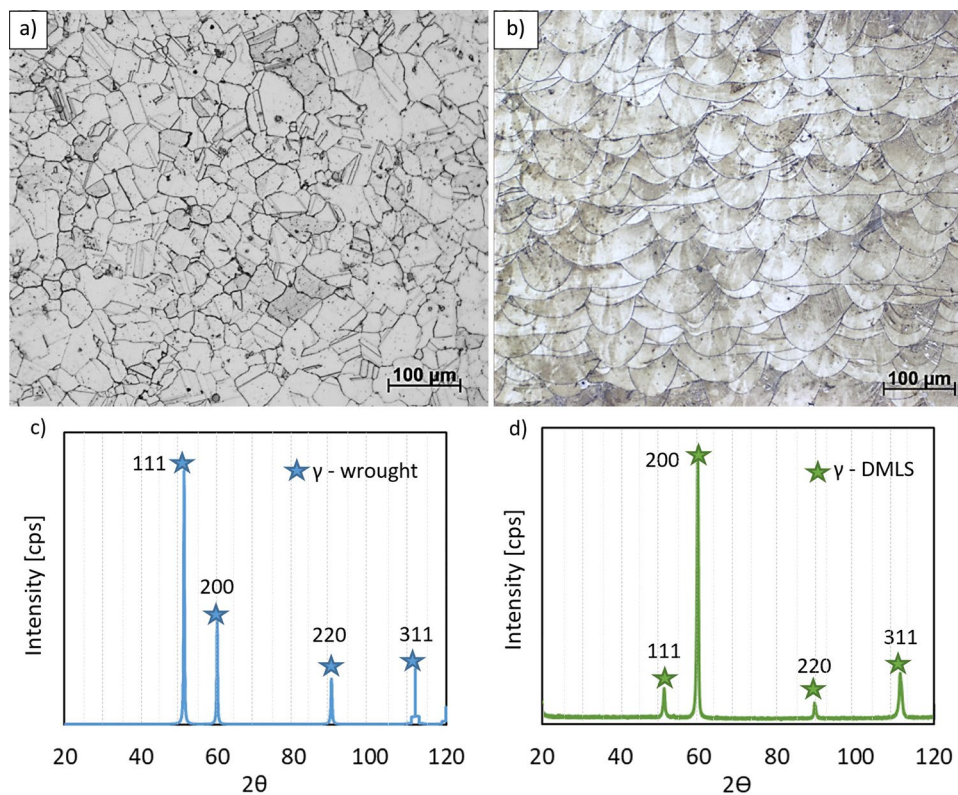
In the following steps, the high-temperature oxidation resistance was assessed through the heat resistance test at 1000°C for 100 h in an air atmosphere. Round bars were wire cut to cylinder specimens of 10 mm in diameter and 2 mm. In order to minimize the overheating effects related to the building of the first and last layers, only round cylinders extracted from the middle section of the 50 mm long bars were used. Five DMLS manufactured and five wrought were used in the experiment. Specimens were removed from the furnace one by one after reaching the specific time of high temperature exposure equal to 1 h, 5 h, 25 h, 50 h and 100 h. An oxidation kinetics were determined based on the measurements of scale thickness as well as the depth of the diffusion zone after a specific time of the heat treatment. Finally, a qualitative chemical composition analysis and element distribution maps were performed on cross-sections of both, DMLS and wrought specimens, by using a JEOL6360LA scanning electron microscope (SEM) operated at 20 kV with EDS detector. The metallographic specimens were prepared by conventional procedures including hot mounting, grinding and polishing. After the mounting, the specimens were ground by using a Struers® polishing machine and 600, 800, 1200 and 4000 SiC graded papers and polished on Metrep® Durasilk M cloth. The initial microstructures were observed by using Nicon MA220 optical microscope. The XRD measurements were performed using a Rigaku (Tokyo, Japan) Ultima IV diffractometer with Co-K radiation ($\lambda = 1.78897$ Å) and operating parameters of 40 mA and 40 kV with a scanning speed of 1°/min and a scanning step of 0.02° in the range of 20°–120°. Additionally, to analyse the phase of oxidation products in the scale layer as a function of the depth from the specimen surface, XRD analysis was performed using the grazing incident X-ray diffraction (GI XRD) technique for incidence angles of 1, 2 and 5° based on Co radiation Kα1 ($\lambda = 1.78892$ Å) using the Rigaku Ultima IV system with parallel beam mode.

Results

The initial microstructure of wrought and AM Haynes 282

The microstructure of as-received, wrought Haynes 282 is presented in Fig. 2a. It consists of large austenite grains and twins. On the other hand, the

microstructure of DMLS Haynes 282 was characterized by a multilayer structure of melting pools in which a dendritic structure formed of columnar grains oriented along the building direction (Fig. 2b), which is a characteristic for additively manufactured nickel-based superalloys [19]. The mechanical properties and oxidation resistance of Haynes 282 depend on the formation of secondary phases in the microstructure including carbides and gamma prime. These carbides have the form $M_{23}C_6$ rich in chromium, nickel, cobalt, and molybdenum or M_6C rich in molybdenum, nickel or chromium [13]. The γ' phase, rich in nickel and aluminium, forms a coherent precipitate structure within the γ matrix, which helps maintain the alloy's mechanical integrity and surface stability at high temperatures. These secondary phases contribute to the formation of a protective oxide layer, primarily consisting of chromium and aluminium oxides, which acts as a barrier to oxygen diffusion, thereby enhancing the alloy's resistance to oxidation. The presence and stability of these phases are critical, as they reduce the rate of oxidation by limiting the diffusion pathways for oxygen and other oxidizing species, thus prolonging the material's lifespan in harsh environments [20]

The XRD graphs were used to reveal phase structures for both states of Haynes 282. Intensity peaks identified for wrought material (Fig. 2c) according to card 01-074-5256 revealed a solid solution of aluminium in nickel (γ) (Al0.14 Ni0.86) in different configurations (111), (200), (220) and (311) for angles equal to 51.2, 59.8, 89.72 and 111.46, respectively. On the other hand, peaks for DMLS-manufactured material suggested aluminium nickel (Ni0.852 Al0.148) in different configurations (111), (200), (220), (311) and (222) for angles equal to 51.32, 59.92, 90, 112 and 119.96, respectively (04-024-6816). The differences in peaks were associated with strong texture found for DMLS material. It suggests that grains have specific orientation of 200 associated with the printing direction.

XRD phase analysis of oxidized surfaces

The high-temperature exposure of wrought Haynes 282, even for a relatively short time as 1h, led to the formation of multiple phases mainly consisting of chromium, titanium and aluminium oxides (Fig. 3a). The intensity of peaks corresponding to particular phase does not change significantly after 100h, however, the variety of newly formed phases could be observed when the XRD was examined under a lower angle (Fig. 4a). The measurement performed under 1°–2° exposed the occurrence of chromium oxide (Cr_2O_3) on the specimen surface suggesting it formation already in the first stages of high temperature exposure. Furthermore, below the surface, the considerable growth of titanium oxides (TiO_2 and Ti_5O_9) was found when the measuring angle was equal to 5°.

Additionally, the formation of spinels was observed. These phases involve mainly three compounds: $TiCr_2O_5$, $Ti_4Cr_2O_5$, and $Ti_{0.24}Cr_{1.76}O_3$.

DMLS-manufactured Haynes 282 was characterized by different oxidation behaviour. Once exposed to the high temperature, the rapid formation of intermetallic phases (NiAl and Ni_3Al) and a small share of different metallic oxides (TiO_2 and presumably Al_2O_3) was observed (Fig. 3b). The prolonged 100h high temperature exposure at 1000 °C led to the growth of chromium (Cr_2O_3) and aluminium (Al_2O_3) oxides. The XRD measurements performed just beneath the specimen surface using low angles of 1° and 2° revealed a considerable share of different, non-stable titanium and chromium oxides: $Ti_{0.92}Cr_{0.08}O_{1.96}$ and $Ti_{0.24}Cr_{1.76}O_3$ (Fig. 4b). Subsequent examinations performed under an angle equal to 5° exposed the substantial growth of titanium oxides. The list of phases with corresponding card numbers defined during XRD measurements was presented in Appendix A.

One should stress, that oxidation kinetics varied significantly as the high-temperature exposure led to the formation of many unstable oxides in DMLS material. On the other hand, the high microstructural stability was confirmed for wrought Haynes 282, as shown in Fig. 3. Nevertheless, it could be easily observed, how the phase composition changes when different measuring angle is applied. The measurements executed at the lowest angle equal to 1° provide essential information about the phases formed just on the specimen surface. The higher the measuring angle is, the deeper material layers are investigated. It could be found, that for AM material, there is a considerable share of chromium oxides, which is directly related to the formation of the Cr_2O_3 on the surface. When the measuring angle was increased, some titanium and aluminium oxides were detected. One should note, that for DMLS Haynes 282, the extension of the high temperature exposition time to 100h results in the formation of the greatest share of various titanium oxides in comparison with the wrought material. The intensity of peaks from chromium and titanium oxides is changing effectively with the progressing oxidation.

Figure 3 The XRD graph of wrought (**a**) and DMLS manufactured (**b**) Haynes 282 after 1h and 100h of high-temperature exposure at 1000°C.
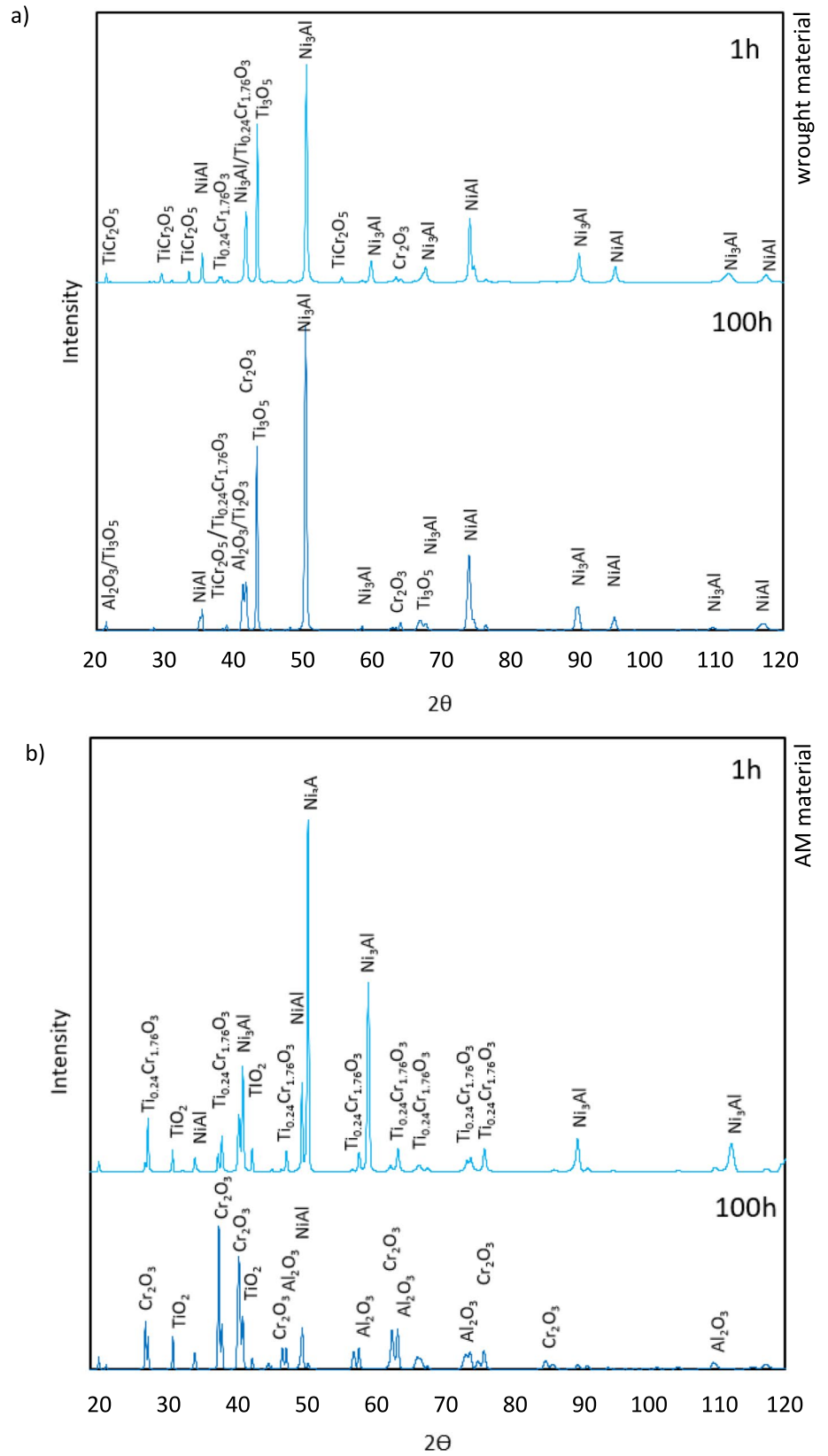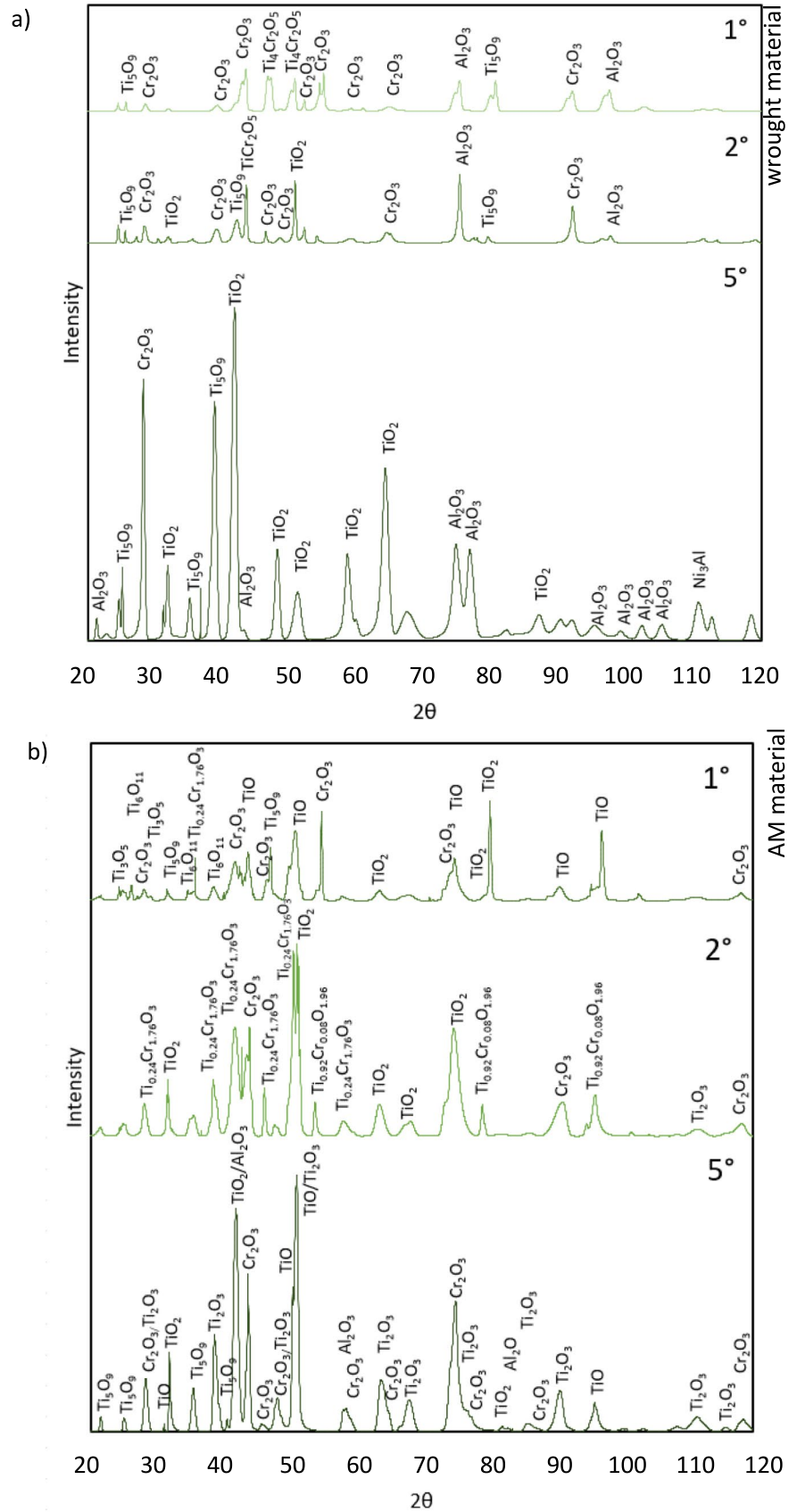
Figure 4 The XRD graph of wrought (**a**) and DMLS manufactured (**b**) Haynes 282 after 100h of high-temperature exposure at 1000°C performed under various angles.

Surface topography observations

The microstructural observations were performed on the oxidized surfaces to investigate the tightness of the formed scale (Fig. 5). One could find, that AM material has a more developed surface than the wrought one. Even short-time exposure of 1 h at 1000°C led to the formation of oxides. It should be stressed, that the low structural stability confirmed by the XRD analysis is responsible for the growth of numerous non-stable oxides. These newly formed compounds of high brittleness are poorly connected with the base material since many cracks appear on the micrographs. The extended high-temperature exposure led to the further development of the surface. The substantial growth of titanium oxides was observed when the

Figure 5 The surface morphology of additively manufactured and wrought Haynes 282 after oxidation.
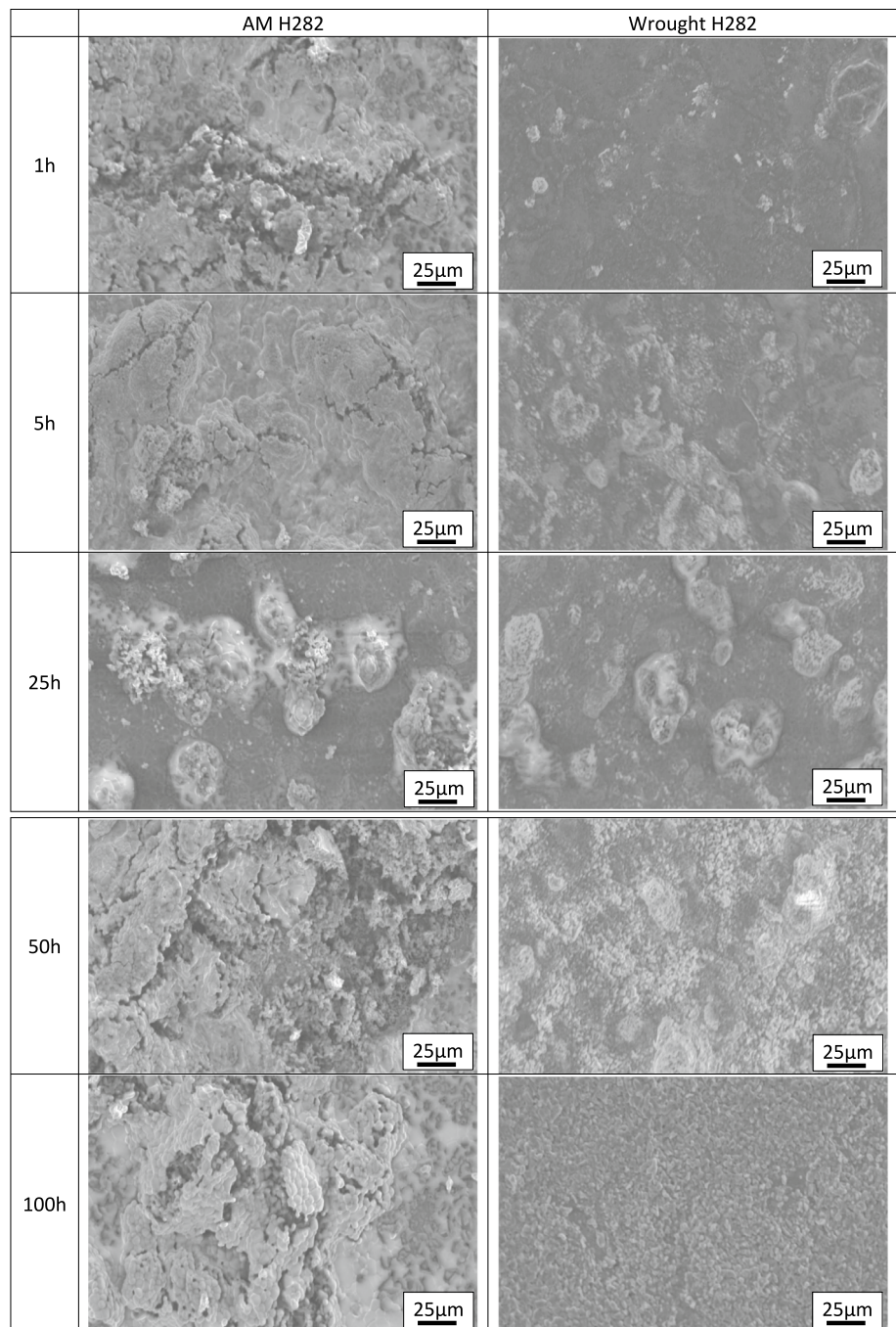
high temperature exposure time exceeded 50 h. On the other hand, stable growth of chromium oxides was observed for wrought material (Figs. 3 and 4). The progressing exposure time led to the formation of a relatively smooth and uniform protective scale. In order to confirm whether AM material is prone to accelerated oxidation, further analysis was performed on the cross-sections of specimens presented in Fig. 6.

Qualitative microstructural analysis on the Haynes 282 cross-sections

The notably different cross-sectional views of the wrought and DLMS specimens subjected to exposure at 1000 °C for 1h exposed various mechanisms responsible for high temperature oxidation behaviour of Haynes 282 (Fig. 6). It was observed, that AM specimen was characterized by four diffusion regions while wrought one was protected by single-layered, tight scale of the oxide. The increased content of chromium and oxygen in areas marked as 1 and 2 confirmed the formation of Cr_2O_3 detected during XRD analysis (Table 2, Figs. 4 and 5). Subsequent analysis

performed in areas 3 and 4 suggests the formation of aluminium and titanium oxides (presumably Al_2O_3 and TiO_2) as well as NiAl intermetallic phases (Fig. 6). The relatively short high temperature exposure time of 1h was sufficient to initiate the segregation of elements on the grain boundaries of additively manufactured material. On the other hand, the brittle protective scale of $< 10\mu m$ composed of metallic oxides was formed on the surface of wrought Haynes 282 (area 6, Fig. 6). Just below this scale, a very thin Cr_2O_3 chromium oxide layer was formed (area 7, Fig. 6). Considerable pitting effects were also observed below the surface. The chemical analysis performed in these areas suggests the segregation of aluminium (Table 2). One should observe, that wrought material possesses higher structural stability at high temperature since just a very thin and tight protective layer was formed.

The observations performed on the wrought and AM specimens after 100h reveal the drastic impact of high temperature on DMLS specimens surface. The thickness of formed layers changes considerably. The chemical composition analysis executed 5μm below the surface reveals the high content of titanium and

Figure 6 The cross-sectional view of additively manufactured and wrought Haynes 282 after 1 h exposure to 1000°C.
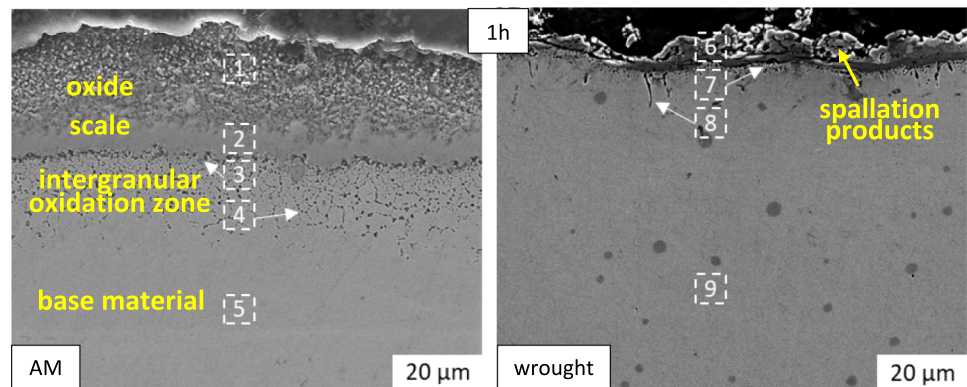

Table 2 The chemical composition of specific areas of additively manufactured and wrought Haynes 282 after 1 h of exposure to 1000 °C (wt.%)

Wt.%	Element	O	Al	Cr	Ti	Ni	Co	Mo
AM	1	9.9	1.6	75.3	5.2	5.1	2.9	–
	2	15.5	1.6	69.0	3.8	8.0	–	02.1
	3	3.3	0.8	13.2	0.8	58.2	11.8	11.9
	4	18.6	72.9	1.5	1.1	4.0	1.9	-
	5	1.0	1.6	19.3	2.00	57.2	10.4	8.5
Wrought	6	11.8	3.3	37.4	06.6	23.3	16.7	0.9
	7	13.4	0.9	71.7	4.6	7.6	1.3	0.5
	8	5.4	20.4	9.5	0.9	48.2	9.3	6.3
	9	0.9	1.7	19.2	02.2	56.5	10.8	8.7

Figure 7 The cross-sectional view of additively manufactured and wrought Haynes 282 after 100 h of exposure to 1000 °C.
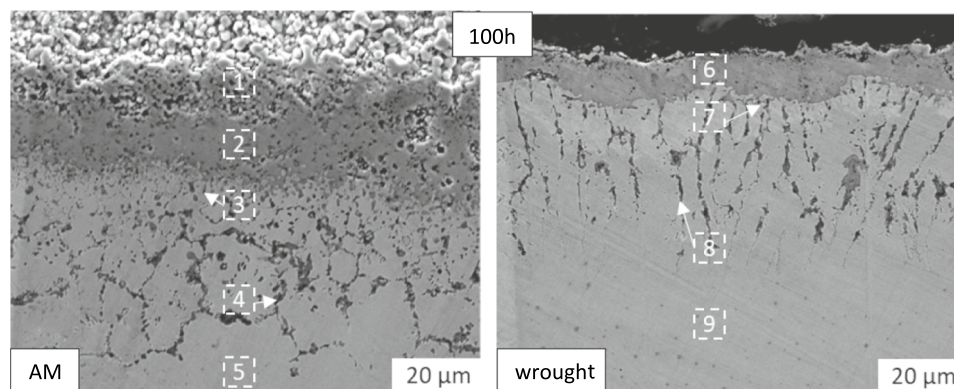

Table 3 The chemical composition of specific areas of additively manufactured and wrought Haynes 282 after 100 h of exposure to 1000 °C (wt.%)

Wt.%	Element	O	Al	Cr	Ti	Ni	Co	Mo
AM	1	12.0	0.2	7.6	79.0	0.6	0.3	0.3
	2	15.0	0.9	75.0	7.5	1.1	0.5	-
	3	7.6	14.3	13.4	21.2	34.5	6.8	2.2
	4	19.8	71.6	1.7	1.1	4.0	1.8	-
	5	0.8	0.7	14.3	2.8	61.7	11.2	8.5
Wrought	6	14.0	0.7	78.9	3.4	1.9	0.7	0.4
	7	3.9	9.7	10.7	6.8	49.8	9.1	10.0
	8	15.6	36.6	3.6	31.1	8.8	1.9	2.4
	9	1.0	1.5	18.3	1.9	57.8	10.9	8.6

aluminium (Fig. 7, Table 3). It should be noticed, that titanium oxides were not dominant during the initial XRD scan (Fig. 3b), however, the measurements performed under low angle exposed the high share of different titanium oxides in the area marked as 1 (Fig. 4b). Below the layer of titanium oxide, the tight layer of chromium oxide could be found (area 2, Table 3, Fig. 7). Similarly, aluminium and titanium oxides tend to form preferentially along grain boundaries (Table 3, Fig. 7). The high temperature oxidation behaviour for wrought material was completely different. The growth of a tight, protective chromium oxide scale (area 6) was followed by the formation of a dendritic structure in which elongated grains were surrounded by aluminium and titanium oxides.

The subsequent EDS maps exposing element distribution after a particular time of high temperature exposure were used to confirm the diffusion kinetics responsible for high-temperature oxidation of Haynes 282 in wrought and DMLS conditions (Figs. 8 and 9). One should highlight, that regardless of the material state (wrought/DMLS manufactured), a similar

behaviour could be observed. It involves the diffusion of oxygen, titanium and chromium to the surface and the segregation of aluminium on the grain boundaries just below it. This phenomenon is, however, more prominent for DMLS material since the formation of aluminium oxide on the grain boundaries and uneven distribution of titanium below the surface was observed (Fig. 8).

Additionally, intergranular oxidation was found for DMLS Haynes 282 represented by the segregation of aluminium and oxygen and depletion of nickel on the grain boundaries (Fig. 8). Based on the cross-sectional micrographs, one can find, that the depth of such intergranular oxidation after 100h was about 50μm and decrease with higher material density (Fig. 7). Similar observations were observed for Inconel 718 manufactured by using SLM and subjected to high temperature exposure at 850 °C for 100h [21]. The comparative studies of AM and wrought Inconel 718 present that the oxidation kinetics of the as-built LBM 718 alloy is much higher, even for the densest samples [22].
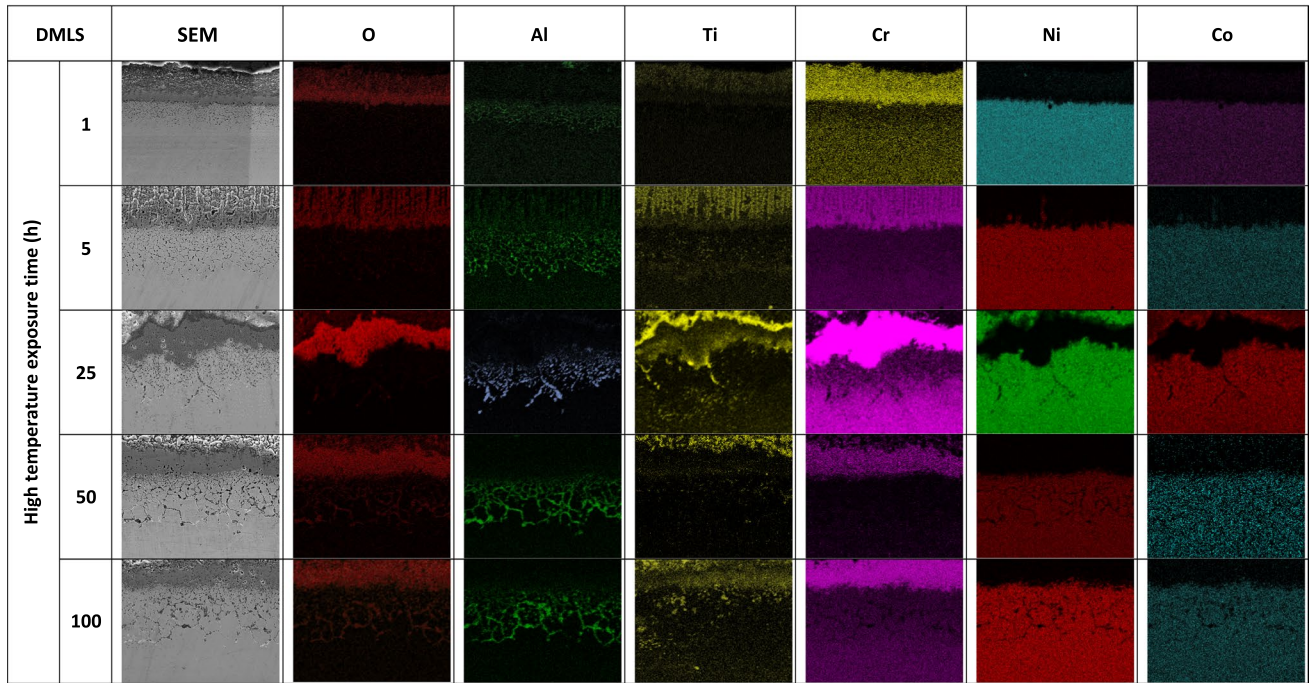
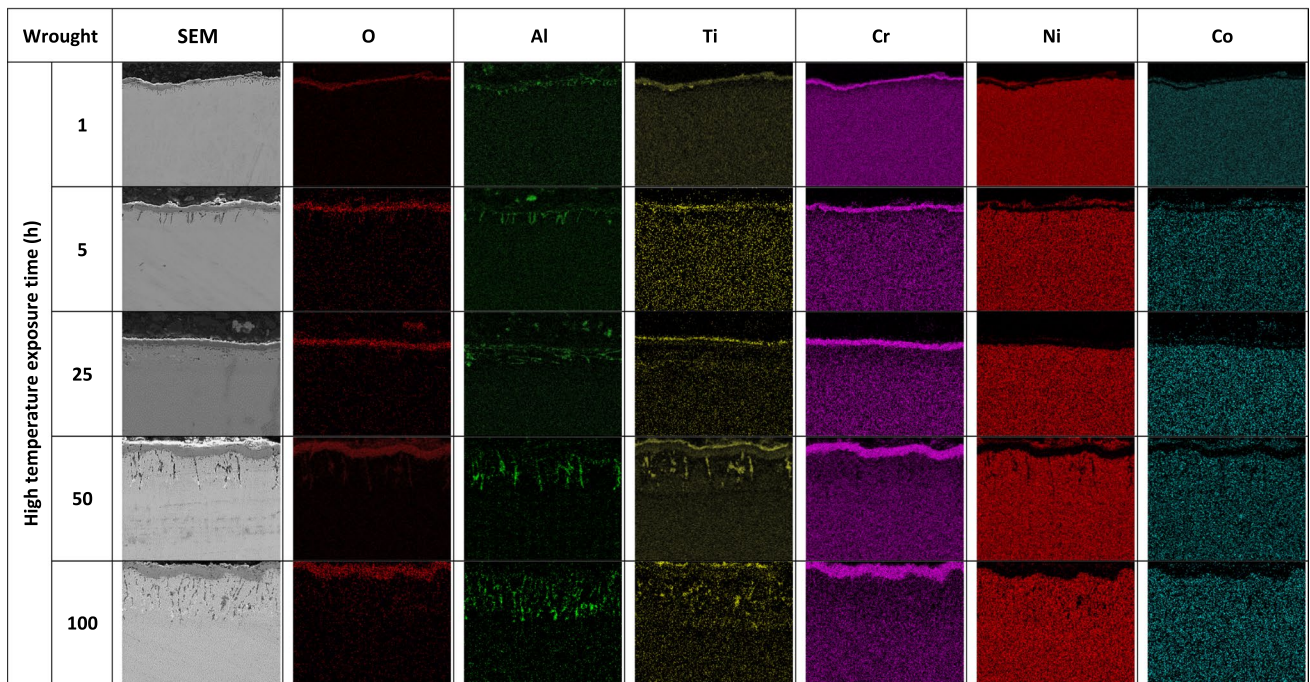**Figure 8** The element distribution of additively manufactured Haynes 282 after exposure to 1000°C.

Figure 9 The element distribution of wrought Haynes 282 after exposure to 1000 °C.

Discussion

One should highlight the higher structural stability of wrought material in comparison with AM one. It is widely reported, that nickel-based superalloys are prone to oxide spallation in air at 1000 °C [23]. Such spallation is more prominent for AM material because of the formation of brittle oxides. The rate of their growth clearly indicates faster oxidation kinetics of AM Haynes 282 as compared to wrought material, which is directly related to the higher oxygen uptakes [24]. One should mention, that the developed surface of AM nickel-based superalloys with increased roughness or porosity provides more sites for oxide nucleation and growth, which can lead to a non-uniform oxide layer that is more prone to cracking and spallation. Additionally, surface defects such as micro-cracks or pores can act as pathways for oxygen diffusion, accelerating oxidation and compromising the integrity of the protective oxide layer. Such behaviour leads to severe spallation during the oxidation, and in turn, inhibits the growth of tight, protective Cr_2O_3 oxide layer on the surface [25]. Consequently, the formed oxide of high brittleness could only be maintained for a very short period, thus not being effective as a thermal barrier. Such behaviour is leading to the drastic degradation of the surface and sub-surface microstructure since progressing spallation will contribute to the accelerated growth of Ni-rich oxides. Further evolutions involve the transformation of chromium oxides into $Ni(Cr,Fe)_2O_4$ spinel phases, which are not effective as a protective scale [26, 27]. It leads to the expansion of the oxide layer into the material core. Since the subsurface layers have enough chromium, the further diffusion of oxygen will again contribute to the formation of spinels and progressing spallation.

In order to understand the oxidation behaviour of AM and wrought Haynes 282, not only the formation of scale and its characterization should be performed, but also changes that occurred near the surface should be analysed. For such a purpose, the depth of the diffusion zone was measured as well. Such depth was established based on the occurrence of aluminium oxides formed on the grain boundaries.

Based on the microstructural analysis performed by using SEM and XRD, one can define and describe oxidation mechanisms that occurred in DMLS and wrought Haynes 282 after high temperature exposure (Fig. 10). Once the specimens were subjected to 1000 °C, the chemical adsorption between their surfaces and the air atmosphere in the furnace occurred [27]. It results in the formation of the oxide layer on the surface due to selective oxidation of the active elements: titanium for DMLS material and chromium for wrought one (Figs. 8, 9 and 10). Once chemical adsorption between titanium/chromium and oxygen is completed, TiO_2 and Cr_2O_3 oxides are formed. Continuous high-temperature exposure leads to the diffusion of the aluminium atoms on the grain boundaries and subsequent formation of hard aluminium oxides (Fig. 7). The segregation of aluminium oxides as well as the formation of adherent, dense and continuous oxide layers on the surface is leading to the occurrence

Figure 10 The schematics of wrought and DMLS Haynes 282 oxidation during high temperature exposure.
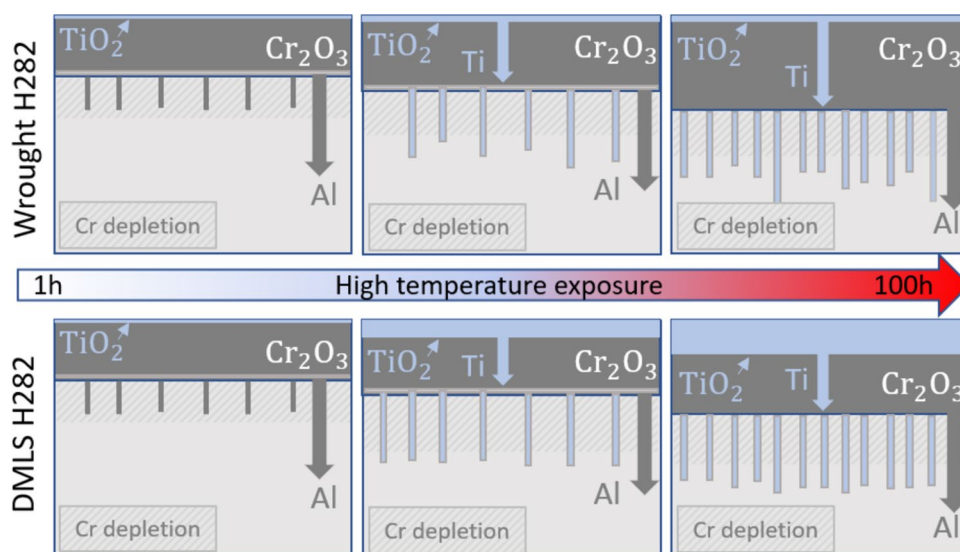
of thermal stress [30]. Once, the accumulated stresses exceed the carrying capacity of the oxidation layer, spallation of brittle areas could be observed (Fig. 10a). It leads to the further diffusion of the chromium and titanium towards the surface and the subsequent formation of their oxides (Figs. 8 and 9). The progressing oxidation is depleting the content of chemically active elements thus degrading the base material.

Based on the changes in oxide layer thickness, high-temperature oxidation behaviour of Haynes 282 was found similar as compared to different Inconel alloys and Haynes 263 [27–29]. It was reported, however, that after prolonged exposure to elevated temperature, this alloy is characterized by a thicker protective oxide layer, which is attributed to the higher concentration of titanium and aluminium [16]. It is further leading to the growth of TiO_2 prior to the formation of Cr_2O_3 due to the susceptibility of these elements to internal oxidation. It should be stressed, that literature reports confirm its desirable oxidation kinetics since it follows parabolic law at temperatures up to 750 °C [16, 28] and quasi-parabolic law up to 1050°C [18].

One can indicate, that the diffusion-controlled oxidation behaviour is mainly driven by the formation of a continuous chromium layer, which acts as a critical barrier for the diffusion of oxygen and/or chromium [17]. The presence of characteristic XRD diffraction peaks of Cr_2O_3 in wrought and DMLS specimens indicates that the diffusion of chromium through the chromium layer significantly influences the oxidation mechanism. The longer high-temperature exposure time is, the thicker the chromium oxide scale is formed and more chromium is depleted from the sub-surface (Figs. 8, 9 and 10). Although chromium is necessary for a protective chromium oxide surface layer formation, its higher content may result in phase instabilities and the development of brittle chromium-rich phases [30, 31]. One should highlight, that in the temperature range between 900 °C and 1200 °C, a higher aluminium content may offer better protection since the growth and diffusion rate of aluminium oxide (Al_2O_3) are slower as compared to chromium oxide (Cr_2O_3) [32]. However, an effective Al_2O_3 layer can form when the aluminium content exceeds 3 wt.%. Since Haynes 282 has a relatively low aluminium volume of about 1.5%, it is not possible to form a protective Al_2O_3 layer.

One should also consider the interactions on grain boundaries due to intergranular oxidation, which can be clearly observed in Figs. 7, 8 and 9. These could be described, although the qualitative EDS mapping

approach was used. After 100h high-temperature exposure at 1000°C, both DMLS and wrought Haynes 282 exhibited an external scale consisting of chromium, as well as intergranular oxides TiO_2 and Al_2O_3. Chromium diffused towards the surface of the alloy, traversing through the grains and grain boundaries, that are recognized as pathways for diffusion, and where it reacted with oxygen to form the external chromium scale [33]. On the other hand, the volume of aluminium and titanium, their concentrations and diffusion coefficients are too low to enable their diffusion towards the surface to create a continuous external layer thus their oxides are formed internally [33]. Finally, one should stress, that the growth of intergranular oxide is facilitated by the rapid diffusion of oxygen along grain boundaries, as well as the subsequent formation of aluminium and titanium oxides on such boundaries. Based on Figs. 7, 8 and 9, it can be concluded, that aluminium and titanium concentrations decreased to zero approximately 60μm from the surface, suggesting diffusion towards the grain boundary to stimulate the growth of intergranular TiO_2 and Al_2O_3. Simultaneously, aluminium atoms diffuse towards the nearest grain boundary and diffuse upward in the grain boundary to react with oxygen. Consequently, the diffusion of titanium and aluminium led to the dissolution of hardening precipitates like γ′, γ″, and δ phases [33].

In order to reveal the oxidation kinetics, the measurements of and thickness of the formed scale (Fig. 11a) and the depth of aluminium diffusion (Fig. 12a) were executed. Subsequently, linear, logarithmic, parabolic and cubic laws were used to represent the data obtained during the measurements. The dominant oxidation kinetics mechanism was then revealed according to the best fit of the square root function. Because of the brittleness of the scale formed after 100h and its subsequent spallation, the measurements at that specific time were not considered during calculations.

The analysis of oxidation kinetics presented in Figs. 11 and 12 confirmed, that the formed scale of DMLS-manufactured Haynes 282 exhibits linear behaviour (Fig. 11b) which corresponds to the formation of a brittle, non-protective oxide scale [34]. On the other hand, tight and adhered scale formed on wrought material was well represented by logarithmic law (Fig. 11c). The oxidation kinetics were also investigated in terms of the depth of aluminium diffusion and its formation on grain boundaries in the form of
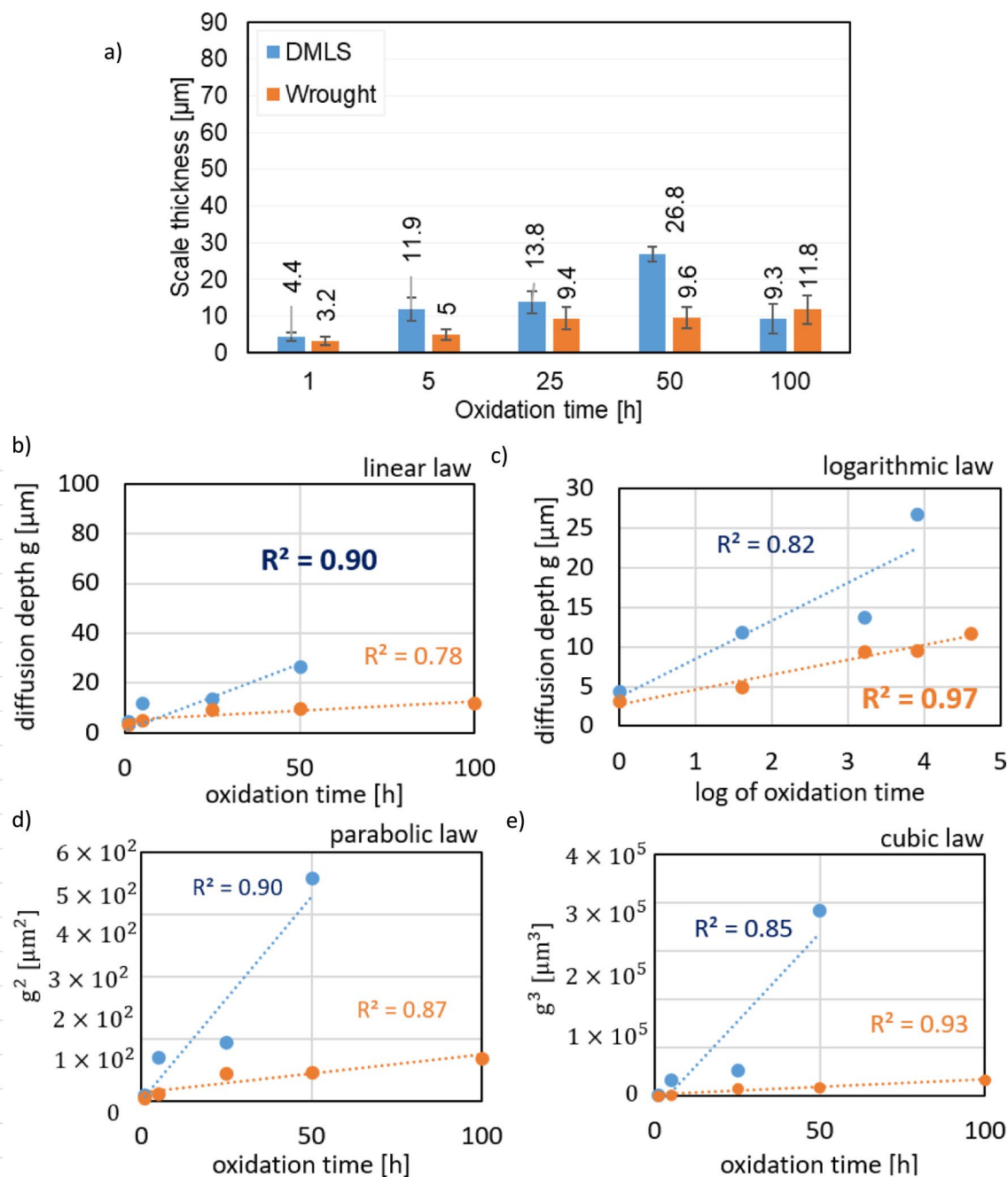
Figure 11 The thickness of scale (**a**); oxidation kinetics based on linear (**b**), logarithmic (**c**), parabolic (**d**) and cubic laws (**e**).

aluminium oxides (Fig. 12). It was found, that DMLS-manufactured material obeys cubic law (Fig. 12e), while wrought one logarithmic (Fig. 12b). One could observe the significant increase of aluminium diffusion depth for DMLS material just after 5h of high-temperature exposure followed by its stabilization up to 100h. On the contrary, wrought Haynes 282 exhibited a steady increase of aluminium diffusion from 1 to 100h.

Based on microstructural observations (Figs. 6, 7, 8 and 9) and changes in scale thickness and depth of the aluminium diffusion zone (Figs. 11 and 12), one can conclude, that the oxidation rate of DMLS Haynes 282 was higher as compared to the wrought alloy. This could be potentially attributed to the smaller grain size of the AM material. The smaller grain size promotes diffusion of aluminium and titanium and faster nucleation of oxides on grain boundaries. Another
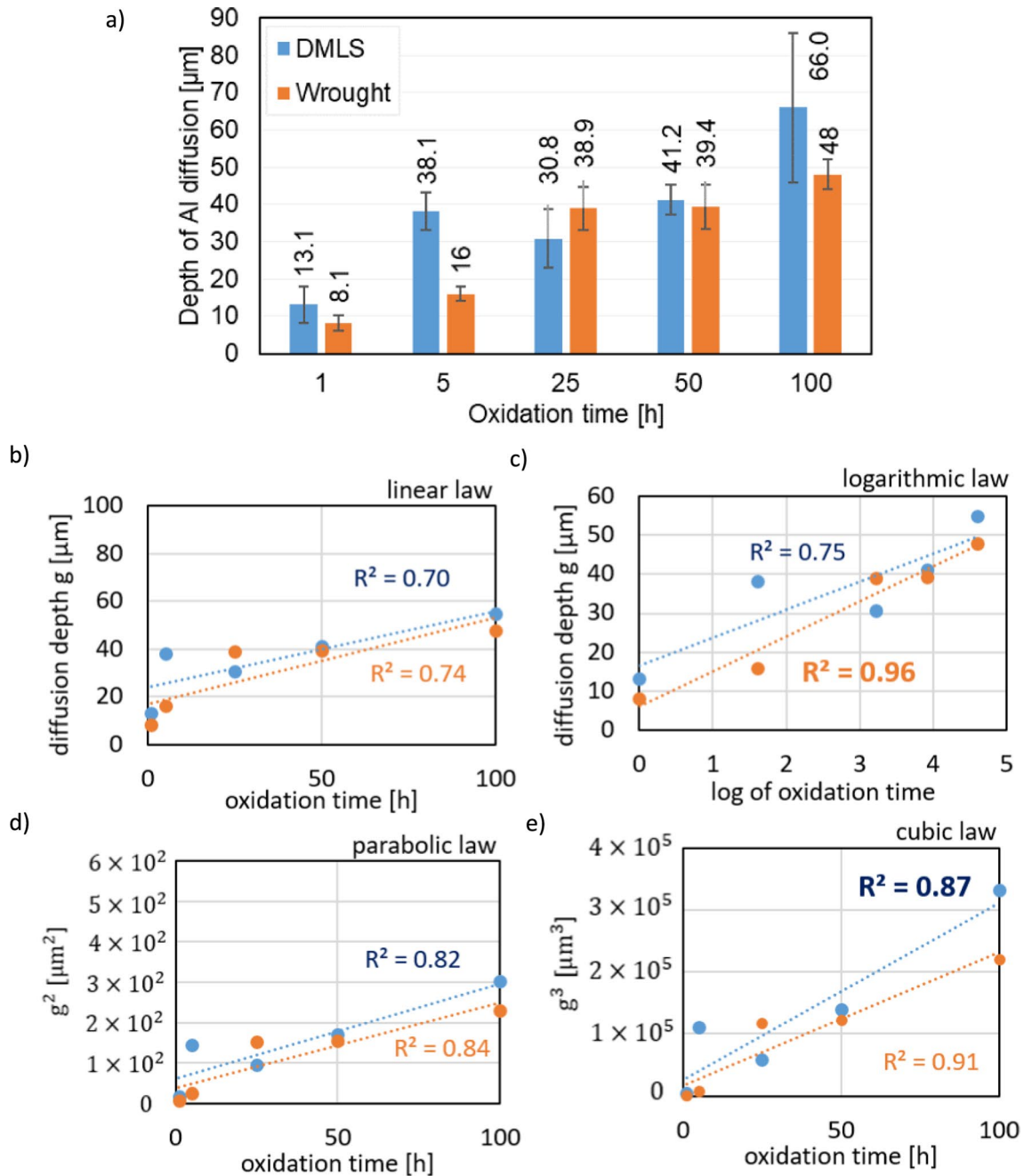
Figure 12 The depth of the diffusion zone (**a**); oxidation kinetics based on linear (**b**), logarithmic (**c**), parabolic (**d**) and cubic laws (**e**.

factor that may influence the oxidation kinetics is the grain boundary diffusion rate. It was reported, that high-angle grain boundaries in nickel-based superalloys provide favourable diffusion paths, and certain crystallographic orientations of nickel oxidize more rapidly due to the faster ion transport [35].

Even though structural stability is much better for the wrought material, some satisfactory results could be found for the DMLS ones. These results suggest, that the applied printing strategy could be beneficial in terms of large-scale component manufacturing. One should consider, however, proper surface machining since high surface roughness can affect the area of the reactive surface and, therefore, the oxidation properties [36]. On the other hand, the higher density of

wrought materials as compared to AM ones would be beneficial for their oxidation resistance.

As mentioned, the DMLS-produced alloy Haynes 282 typically exhibits worse high-temperature oxidation resistance compared to the wrought version due to differences in microstructure and surface finish inherent to the additive manufacturing process. In DMLS, rapid cooling and solidification result in a more heterogeneous microstructure with increased porosity, higher surface roughness, and possibly incomplete or irregular distribution of protective secondary phases like γ' precipitates and carbides. These factors can lead to less effective formation of a continuous and uniform oxide layer on the surface, which is crucial for oxidation resistance. Additionally, the residual stresses and potential presence of micro-cracks in DMLS-produced parts can act as pathways for oxygen ingress, further exacerbating oxidation rates compared to the more homogeneous and refined microstructure typically seen in wrought Haynes 282, which allows for more effective oxide scale formation and improved high-temperature performance. In wrought Haynes 282, the controlled manufacturing process promotes a more uniform distribution of chromium and aluminium, facilitating the formation of a stable, protective oxide layer without compromising phase stability. However, in DMLS-produced alloys, the rapid cooling and inherent process variations can result in uneven distribution and diffusion of these elements, leading to less effective oxide formation. The limited diffusion of aluminium as compared to chromium means that any microstructural inhomogeneities or surface imperfections in DMLS components can initiate localized oxidation, allowing for chromium-depleted zones that form less protective oxides and potentially more brittle phases. This results in the observed differences in corrosion behaviour between DMLS and wrought Haynes 282, despite their identical chemical compositions.

Conclusions

In this paper, the oxidation behaviour of DMLS and wrought Haynes 282 was investigated during high temperature exposure for 100h at 1000 °C. It was found, that the oxidation progress more effectively for AM material since notable growth of titanium oxides could be observed. It is directly related to the low structural stability of AM Haynes 282 and higher oxygen uptakes. The DMLS-manufactured Haynes 282 is characterized by the developed surface topography consisting of different titanium compounds. On the other hand, a relatively smooth and uniform scale of chromium oxide was observed for the wrought material. One should emphasize, that the effective adoption of the DMLS process for Haynes 282 manufacturing requires optimization of process parameters to further produce material with similar or higher strength characteristics as well as possessing high structural stability. Therefore, additional heat treatment should be considered for AM material to avoid undesirable element segregation near the surface during high-temperature exposure.

Acknowledgements

Author contributions

Mateusz Kopec: Conceptualization, Data curation, Formal analysis, Investigation, Methodology, Project administration, Supervision, Validation, Visualization, Roles/Writing—original draft, Writing—review & editing. Izabela Mierzejewska: Data curation, Investigation, Visualization. Dominika Gorniewicz: Investigation, Data curation. Ryszard Sitek: Methodology. Stanisław Jóźwiak: Formal analysis, Investigation, Methodology, Validation.

Data availability

Data will be made available on request.

Declarations

Conflict of interest The authors declare that they have no known competing financial interests or personal relationships that could have appeared to influence the work reported in this paper.

Appendix A

See Table 4

Table 4 The list of phases with corresponding card numbers defined during XRD measurements

Phase name	Card number	Phase name	Card number	Phase name	Card number
Ni_3Al	04–004-7761	Ti_3O_5	04–007-1880	TiO_2	04–008-7849
$NiAl$	04–002-1223	Ti_5O_9	04–005-4351	Cr_2O_3	04–023-4726
Al_2O_3	04–008-3293	Ti_6O_{11}	01–071-0628	TiO	04–005-4347
M_3O_5 ($TiCr_2O_5$)	04–010-0654	M_6O_5 ($Ti_4Cr_2O_5$)	04–010-9345	MO_2 ($Ti_{0.92}Cr_{0.08}O_{1.96}$)	04–026-4380
M_2O_3 ($Ti_{0.24}Cr_{1.76}O_3$)	04–015-9779				

References

[1] Barwinska I, Kopec M, Kukla D, Senderowski C, Kowalewski ZL (2023) Thermal barrier coatings for high-temperature performance of nickel-based superalloys: a synthetic review. Coatings 13:769. https://doi.org/10.3390/coatings13040769

[2] Unocic K, Kirka M, Cakmak E, Greeley D, Okello A, Dryepondt S (2020) Evaluation of additive electron beam melting of Haynes 282 alloy. Mater Sci Eng A 772:138607. https://doi.org/10.1016/j.msea.2019.138607

[3] Zielińska M, Yavorska MR, Poręba M, Sieniawski J (2010) Thermal properties of cast nickel based superalloys. Arch Mater Sci Eng 44:35–38

[4] Sowa R, Arabasz S, Parlinska Wojtan M (2016) Classification and microstructural stability of high generation single crystal nickel-based superalloys. Zaštita Materijala 57(2):274–281. https://doi.org/10.5937/ZasMat1602274S

[5] Shaikh AS, Schulz F, Minet-Lallemand K, Hryha E (2021) Microstructure and mechanical properties of Haynes 282 superalloy produced by laser powder bed fusion. Mater Today Commun 26:102038. https://doi.org/10.1016/j.mtcomm.2021.102038

[6] Fu R, Zhao S, Wang Y, Li Q, Ma Y, Lin F, Chi C (2016) The microstructural evolution of Haynes 282 alloy during long-term exposure tests. Energy materials 2014. Springer, Cham

[7] Ramakrishnan A, Dinda GP (2019) Microstructure and mechanical properties of direct laser metal deposited Haynes 282 superalloy. Mater Sci Eng A 748:347–356. https://doi.org/10.1016/j.msea.2019.01.101

[8] Uriati F, Nicoletto G, Lutey AHA (2021) As-built surface quality and fatigue resistance of Inconel 718 obtained by additive manufacturing. MDPC 3:228. https://doi.org/10.1002/mdp2.228

[9] Ghiaasiaan R, Ahmad N, Gradl PR, Shao S, Shamsaei N (2022) Additively manufactured Haynes 282: effect of unimodal vs. bimodal γ'- microstructure on mechanical properties. Mater Sci Eng A 831:142234. https://doi.org/10.1016/j.msea.2021.142234

[10] Karmuhilan M, Kumanan S (2022) A review on additive manufacturing processes of Inconel 625. J Mater Eng Perform 31:2583–2592. https://doi.org/10.1007/s11665-021-06427-3

[11] Riza SH, Masood SH, Wen C (2014) Laser-assisted additive manufacturing for metallic biomedical Scaffolds. Comprehensive materials processing, vol 10. Elsevier, Amsterdam, pp 285–301

[12] Otto R, Brøtan V, Carvalho PA, Reiersen M, Graff JS, Sunding MF, Åsberg O, Diplas S, Azar AS (2021) Roadmap for additive manufacturing of HAYNES® 282® superalloy by laser beam powder bed fusion (PBF-LB) technology. Mater Des 204:109656. https://doi.org/10.1016/j.matdes.2021.10965

[13] Maj P, Bochenek K, Sitek R, Koralnik M, Jonak K, Wieczorek M, Pakieła Z, Mizera J (2023) Comparison of mechanical properties and structure of Haynes 282

consolidated via two different powder metallurgy methods: laser powder bed fusion and hot pressing. Arch Civ Mech Eng 23:130. https://doi.org/10.1007/s43452-023-00674-y

[14] Kopec M, Liu X, Kukla D, Sitek R, Kowalewski ZL (2023) Effect of printing direction on fatigue response and damage development in additive manufactured Haynes 282 nickel superalloy. Int J Damage Mech. https://doi.org/10.1177/10567895231204951

[15] Magnin C, Islam Z, Elbakhshwan M, Brittan A, Thoma DJ, Anderson MH (2022) The performance of additively manufactured Haynes 282 in supercritical CO_2. Mater Sci Eng A 841:143007. https://doi.org/10.1016/j.msea.2022.143007

[16] Pérez-González FA, Garza-Montes-de Oca NF, Colás R (2014) High temperature oxidation of the Haynes 282© nickel-based superalloy. Oxid Met 82:145–161. https://doi.org/10.1007/s11085-014-9483-6

[17] Tung H-M, Chen T-L, Lan K-C, Liu P-W, Li Y-C (2024) The incipient oxidation behaviors of Haynes 282 at high temperatures. Mater Chem Phys 316:129109. https://doi.org/10.1016/j.matchemphys.2024.129109

[18] Nnaji RN, Bodude MA, Osoba LO, Fayomi OS, Ochulor FE (2019) Study on high-temperature oxidation kinetics of Haynes 282 and Inconel 718 nickel-based superalloys. Int J Adv Manuf Technol 106:1149–1160. https://doi.org/10.1007/s00170-019-04290-0

[19] Majchrowicz K, Pakieła Z, Kaminski J, Płocinska M, Kurzynowski T, Chlebus E (2018) The effect of rhenium addition on microstructure and corrosion resistance of Inconel 718 processed by selective laser melting. Metall Mater Trans A 49:6479–6489. https://doi.org/10.1007/s11661-018-4926-3

[20] Guo C, Li G, Li S, Hu X, Lu H, Li X, Xu Z, Chen Y, Li Q, Lu J, Zhu Q (2023) Additive manufacturing of Ni-based superalloys: residual stress, mechanisms of crack formation and strategies for crack inhibition. Nano Mater Sci 5(1):53–77. https://doi.org/10.1016/j.nanoms.2022.08.001

[21] Jia Q, Gu D (2014) Selective laser melting additive manufactured Inconel 718 superalloy parts: high-temperature oxidation property and its mechanisms. Opt Laser Technol 62:161–171. https://doi.org/10.1016/j.optlastec.2014.03.008

[22] Greene GA, Finfrock CC (2001) Oxidation of Inconel 718 in air at high temperatures. Oxid Met 51:505–521. https://doi.org/10.1023/A:1010359815550

[23] Chyrkin A, Huczkowski P, Shemet V, Singheiser L, Quadakkers WJ (2011) Sub-scale depletion and enrichment processes during high temperature oxidation of themnickel base alloy 625 in the temperature range 900–1000 °C. Oxid Met 75:143–166. https://doi.org/10.1007/s11085-010-9225-3

[24] Chyrkin A, Gunduz KO, Fedorova I, Sattari M, Visibile A, Halvarsson M, Froitzheim J, Stiller K (2022) High-temperature oxidation behavior of additively manufactured IN625: effect of microstructure and grain size. Corros Sci 205:110382. https://doi.org/10.1016/j.corsci.2022.110382

[25] Sun Y, Chen L, Li L, Ren X (2020) High-temperature oxidation behavior and mechanism of Inconel 625 super-alloy fabricated by selective laser melting. Opt Laser Technol 132:106509. https://doi.org/10.1016/j.optlastec.2020.106509

[26] Zheng L, Zhang M, Dong J (2010) Oxidation behavior and mechanism of powder metallurgy Rene95 nickel based superalloy between 800 and 1000 C. Appl Surf Sci 256(24):7510–7515. https://doi.org/10.1016/j.apsusc.2010.05.098

[27] Li D-S, Dai Q-X, Cheng X-N, Wang R-R, Huang Y (2012) High-temperature oxidation resistance of austenitic stainless steel Cr18Ni11Cu3Al3MnNb. J Iron Steel Res Int 19:74–78. https://doi.org/10.1016/S1006-706X(12)60103-4

[28] Clarke DR (2002) Stress generation during high-temperature oxidation of metallic alloys. Curr Opin Solid State Mater Sci 6(3):237–244. https://doi.org/10.1016/S1359-0286(02)00074-8

[29] Gianfrancesco DA (2016) Materials for ultra-supercritical and advanced ultra-supercritical power plants. Materials for ultra-supercritical and advanced ultra-supercritical power plants. Woodhead Publishing, Duxford, UK

[30] Mahaffey JT (2017) Effect of partial pressure of oxygen and activity of carbon on the corrosion of high temperature alloys in s-CO2 environments, University of Wisconsin-Madison

[31] Pike LM, Srivastava SK (2008) Oxidation behavior of wrought gamma-prime strengthened alloys. Mater Sci Forum 595:661–671. https://doi.org/10.4028/www.scientific.net/MSF.595-598.661

[32] Ouyang G, Palasyuk O, Singh P, Ray PK, Deodeshmukh V, Cui J, Johnson DD, Kramer MJ (2024) Predictive design of novel nickel-based superalloys beyond Haynes 282. Acta Mater 275:120045. https://doi.org/10.1016/j.actamat.2024.120045

[33] Sanviemvongsak T, Monceau D, Desgranges C, Macquaire B (2020) Intergranular oxidation of Ni-base alloy 718 with a focus on additive manufacturing. Corros Sci 170:108684. https://doi.org/10.1016/j.corsci.2020.108684

[34] Jača E, Hotař A, Pešička J (2023) Oxidation properties of complex concentrated alloys FeAlCrV and FeAlCrMo. J Mater Sci 58:9025–9037. https://doi.org/10.1007/s10853-023-08571-8

[35] Atkinson A (1988) Wagner theory and short circuit diffusion. Mater Sci Technol 4(12):1046–1051

[36] Ramenatte N, Vernouillet A, Mathieu S, Vande Put A, Vilasi M, Monceau D (2020) A comparison of the high-temperature oxidation behaviour of conventional wrought and laser beam melted Inconel 625. Corros Sci 164:108347. https://doi.org/10.1016/j.corsci.2019.108347

Publisher's Note Springer Nature remains neutral with regard to jurisdictional claims in published maps and institutional affiliations.